Fuel 167 (2016) 295–305

Contents lists available at ScienceDirect

Fuel

journal homepage: www.elsevier.com/locate/fuel

Droplet combustion characteristics of algae-derived renewable diesel, conventional #2 diesel, and their mixtures

Yuhao Xu [a], Ivan Keresztes [b], Anthony M. Condo Jr. [b], Dan Phillips [c], Perrine Pepiot [a], C. Thomas Avedisian [a,*]

[a] Sibley School of Mechanical and Aerospace Engineering, Cornell University, Ithaca, NY 14853, USA
[b] Department of Chemistry and Chemical Biology, Cornell University, Ithaca, NY 14853, USA
[c] Solazyme Inc., 225 Gateway Blvd, San Francisco, CA 94080, USA

HIGHLIGHTS

- Droplet combustion characteristics of algal HRD are compared with DF2.
- Burning rates of algal HRD and R50 droplets are very close to those of DF2 in spite of chemical and sooting differences.
- HRD flames are less bright, suggesting less soot produced, than those of DF2.
- HRD may be an attractive additive and potential drop-in replacement for DF2 alone, or when blended.

ARTICLE INFO

Article history:
Received 28 August 2015
Received in revised form 8 November 2015
Accepted 11 November 2015
Available online 17 November 2015

Keywords:
Algae
Droplet combustion
Spherical symmetry
Algae-derived fuel
Diesel
Blending

ABSTRACT

Fuels derived from bio-feedstocks have received significant attention for their potential to reduce the consumption of petroleum-based liquid fuels, either through blending or direct use. Biofuels produced from heterotrophic microalgae are particularly attractive because of fast conversion of sustainable plant sugars into renewable oils of controllable quality and composition, but without the need for sunlight or carbon from the atmosphere for growth.

This paper describes the results of a fundamental study of the combustion characteristics of hydroprocessed renewable diesel fuel (HRD) produced from this strain of algae, and the results are compared to #2 diesel fuel (DF2) and an equi-volume mixture of HRD and #2 diesel (R50) as representative of blending. A canonical combustion configuration is used for a liquid fuel consisting of an isolated droplet burning with spherical symmetry and with fuel transport being entirely the result of evaporation at the droplet surface. This fundamental liquid fuel burning configuration is conducive to articulating the evaporation and sooting dynamics involved.

The results show that combustion rates and relative positions of the flame and soot aggregates to the droplet surface of HRD droplets are quite close to R50 and DF2 in spite of their significant chemical and sooting differences. These trends are explained based on similarities in the thermal properties of the fuels. Sooting propensity of #2 diesel is greater than that of HRD, with the mixture falling qualitatively in-between. The results suggest that HRD derived from heterotrophic microalgae can potentially be considered a drop-in replacement for DF2 or serve as an additive to DF2.

1. Introduction

Liquid fuels derived from bio-feedstocks are advantageous because they are renewable and may be compatible with the existing fuel infrastructure for transportation engines [1]. Such fuels have been produced from various oilseed crops such as sunflower [2], cottonseed [2], corn [3], and soybean [4]. Concerns over land use for feedstock growth have motivated the development of alternative approaches that use marginal land, require less consumable water, and can mitigate emissions of greenhouse gases. In this context, algae is receiving attention as a promising feedstock due to its potential for high production rates, rapid growth cycles, and high lipid content [5].

An attractive strain of algae is heterotrophic algae. This form of algae can be produced in both the presence and absence of light. In dark conditions, the energy for growth comes from organic carbon dissolved in the culture medium, and a supply of CO_2 is not needed.

* Corresponding author.
E-mail address: cta2@cornell.edu (C.T. Avedisian).

http://dx.doi.org/10.1016/j.fuel.2015.11.036
0016-2361/

Nomenclature

C_p	specific heat
D	droplet diameter
D_o	initial droplet diameter
D_s	soot shell diameter
D_f	flame diameter
D_{fiber}	fiber diameter
H	major axis of an AOI ellipse
K	burning rate
k	thermal conductivity
MW	molecular weight
W	minor axis of an AOI ellipse
t	time

Greek letters

v	stoichiometric coefficient
ρ_L	liquid density
Φ_K	defined parameter in Eq. (2)
Φ_F	defined parameter in Eq. (3)

Subscripts

s	soot shell
f	flame
g	gas or vapor state

These advantages alleviate constraints on growing algae that favor geographical regions which receive significant daily light while requiring CO_2. Heterotrophic algae is, therefore, promising as a biofuel feedstock which could meet the fuel needs of the transportation sector since it de-couples oil production from both geography and seasonality.

There are two broad pathways to produce biofuels from algal lipids: trans-esterification and hydrogenation [6]. Trans-esterification of algal oils produces algal "biodiesel" (BD), consisting of long chain fatty acid methyl esters (FAME) [1], and glycerin as a co-product. Hydrotreated renewable diesel (HRD, "green" diesel) is produced by removing oxygen molecules to saturate double bonds [7,8]. While a significant amount of work has been reported on the production and life cycle evaluation of algal BD [6,8–17] and algae-derived HRD [6,8,18,19], little research has been reported on fundamental combustion properties of these fuels. Most desirable outcome for an algae-derived fuel is to be a 'drop-in' replacement [20] for a petroleum fuel. However, information does not currently exist to assess this potentiality.

Most of the reported research on algal biofuels focused on system-level evaluation of HRD and BD. For example, the in-cylinder performance of diesel engines fueled by algae BD [21–23], mixtures with diesel fuel [22–27], and HRD [28,29] was studied. A 50/50 blend of algal HRD with NATO F-76 (similar to #2 Diesel fuel) was also examined in a gas turbine engine [30,31]. Furthermore, a study of marine gas turbines to certify algal biofuels for Navy marine systems [30] showed a connection between engine starts (ignition) and fuel properties, but little else could be extracted from the results that extends beyond the engine used to obtain the information.

Engine tests yield useful information about combustion performance under realistic conditions. However, the environment of an engine is overly complex for extracting fundamental information about mechanisms that control combustion because of the complex turbulent transport present and the time-dependent volume of the combustion zone. The information is often unique to the specific engine design employed in the experiments. A low-dimensional transport configuration for combustion can facilitate the development and interpretation of experimental observations. For a liquid fuel the simplest configuration that still has a connection to liquid spray injection is that of an isolated droplet burning in an environment that promotes spherical symmetry in the gas, with transport processes that arise only as a result of the evaporation of the fuel at the droplet surface [32,33]. Fig. 1 illustrates such a canonical configuration of liquid fuel combustion.

A single stationary isolated droplet is ignited and burns in a quiescent environment without the influence of forced or buoyancy-induced convection. The gas flow is created entirely by the evaporation process. Under these conditions, the streamlines of the flow are radial, resulting in spherical symmetry in the gas phase: the flame is then spherical and concentric with the fuel droplet, and if soot forms, the soot aggregates are trapped between the droplet and the flame where the forces (i.e., due to evaporation-induced velocity and thermophoresis) acting on the soot particles balance [34]. Despite its simplicity, the spherically symmetric droplet burning configuration involves a large number of the physical and chemical processes relevant for the much more complex flows encountered in sprays and engines [35], including unsteady gas and liquid transport, preferential vaporization, moving boundary effects, variable fuel properties, detailed combustion kinetics, soot formation, and radiation effects, making it ideally suitable for model development and validation.

To the authors' knowledge, no experiments have been conducted for algae-based liquid fuels in environments that promote the combustion symmetry depicted in Fig. 1. The present study does so specifically for algae HRD. HRD was selected because it is more widely available than algal biodiesel from trans-esterification, and may have a greater potential for adoption as a transportation fuel due to its chemical characteristics (e.g., energy density, cetane number, storage stability) [36]. In addition, HRD meets the ANSI D975 diesel standard [6,8].

In this paper, the combustion performance of HRD, as measured by the evolution of droplet, soot shell, and flame diameters, is compared with conventional #2 diesel (DF2), and a 50% DF2 and 50% HRD mixture on a volume basis (denoted "R50", to follow prior engine studies [30,31] that evaluated performance of equi-volume mixtures). The experimental methods and chemical analysis are described in Section 2, while the results and subsequent analyses and discussions can be found in Section 3. A summary is provided in Section 4.

2. Experimental methods

2.1. Design

Spherical symmetry is promoted by using "small" droplets with initial diameter D_o between 0.52 and 0.55 mm, restricting their motion by anchoring them to very small support structures (or fibers), employing a stagnant ambient in the experiments, and minimizing the effects of buoyancy by carrying out the experiments at low gravity (on the order of 10^{-4} of normal gravity on Earth). The ambient for the data reported here is air at room temperature and atmospheric pressure. A brief outline of experimental design and procedures is given below. More details are provided in [37–39].

Droplets with the desired size are deployed at the intersection of two SiC fibers (~14 μm diameter) so that the droplet will not move throughout its burning history. Fig. 2a shows a planar view

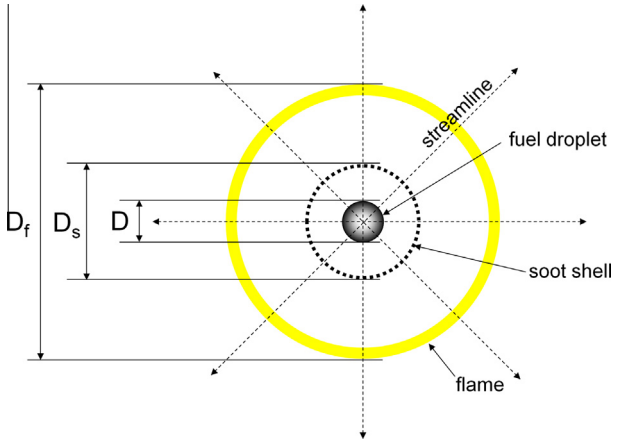

Fig. 1. Schematic of a spherical droplet flame.

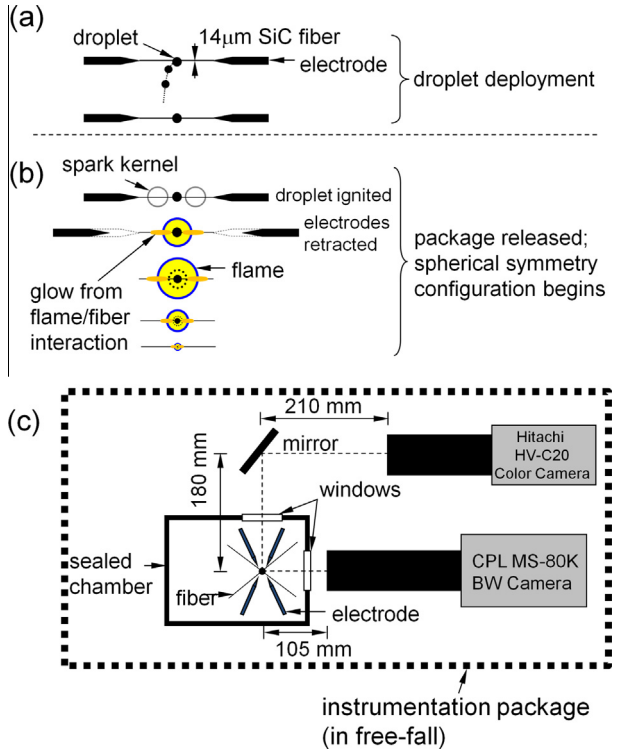

Fig. 2. Schematic of the experimental setup: (a) droplet deployment process, (b) sequence of droplet ignition, retraction of the spark electrodes, and spherical droplet burning process, (c) layout for the combustion chamber and two cameras inside the instrumentation package.

illustrating the process of deploying droplets from a piezoelectric generator onto the fibers. It has previously been shown that the support fiber design used here when coupled with droplets of the initial size employed will minimally influence burning [38,39]. In addition, micro-convective effects, observed for example for fiber-supported 'large' droplets ($D_o > 2$ mm) [38], are not observed in the present study.

Fig. 2b shows the sequence of events for igniting the droplet by a spark and retracting the ignition electrodes. Two sparks are employed and positioned on opposite sides of the droplet in order to promote symmetry in the ignition and subsequent burning process. Each spark requires two electrodes across which the sparks are generated, hence four total electrodes are employed.

Once the droplet of desired size is deployed on the fiber, the instrumentation package is released into free-fall (Fig. 2b) over 7.6 m to provide approximately 1.2 s of experimental run time. The droplet is ignited 320 ms after free fall begins. The sparks are 'on' for 800 μs and then the spark electrodes are rapidly retracted (Fig. 2b). The time sequences are coordinated by a multi-channel digital signal generator (Quantum Composer, QC-9618). The instrumentation package is released immediately after droplet deployment to minimize effects of vaporization prior to ignition [37].

The droplet burning history is recorded by two cameras that provide perpendicular views of the burning droplet (cf. Fig. 2c). A black-and-white (BW) digital high-speed camera (Canadian Photonic Labs, Inc., MS-80K, 2320 × 1722 pixel/frame, operated at 200 fps) records backlit images that highlight droplet and sooting dynamics. The backlighting for BW imaging is provided by a 1-Watt LED lamp (Black Diamond Equip., LTD). A color camera (Hitachi, HV-C20, 640 × 480 pixel/frame, operated at 30 fps) provides self-illuminated flame images. The BW camera is fitted with an Olympus Zuiko 90 mm f/2.0 lens, an Olympus OM Telescopic Extension Tube 65–116 mm (fixed at 100 mm), and a Vivitar MC 2× teleconverter for best magnification, while the color camera is fitted with a Nikkor 135 mm f/2.0 lens and two Kenko 36 mm extension tubes.

2.2. Image analysis

The video images provide the main diagnostic from which measurements of the evolution of droplet (D), soot shell (D_s), and flame (D_f) diameters are extracted. Image-Pro V6.3 (Bethesda, MD) software is used to manually extract D, D_s, and D_f. The analysis involves placing a virtual ellipse around the area of interest (AOI, Fig. 3a). The equivalent diameter is then obtained as $D = (HW)^{0.5}$, where major (H) and minor (W) axes of the virtual ellipse are obtained from the software. The flame diameter is determined by the outer boundary of the observed blue luminous zone (Fig. 3c and d).

A virtual ellipse, rather than a circle, is used to determine boundaries of droplets, soot shells, and flames to obtain equivalent diameters, because an ellipse is a more general shape with more degrees of freedom for positioning than a sphere. Combustion symmetry could sometimes be affected during the burning history such as from the ignition event that could momentarily deform the droplet.

A number of BW images for HRD are also analyzed by a computer-based algorithm developed previously [40]. However, this automated approach for droplet diameter extraction is not used extensively in this study because of the heavy sooting propensities of the fuels examined, especially for DF2 and R50. Instead, manual measurements that involve placing an ellipse to fit the AOI are extensively adopted in the course of data extractions of D, D_s, and D_f for all fuels examined in this study.

In analyzing the droplet images for DF2 and R50 droplets, the droplet boundary is often obscured by soot as shown in Fig. 3b for a DF2 droplet (at 0.3 s after ignition). Three red[1] arrows in Fig. 3b point to visible segments of the droplet boundary which serve as arcs of an ellipse for obtaining equivalent droplet diameter. Such images are analyzed for droplet diameter only when at least two arcs of the droplet boundary can be observed.

A scale factor is applied to the digital images by a 0.794 mm tungsten-carbide calibration ball (Salem Specialty Ball Company) so that the dimensions of droplets, soot shells, and flames obtained from Image-Pro can be converted to millimeter. The ball is

[1] For interpretation of color in Figs. 3 and 8, the reader is referred to the web version of this article.

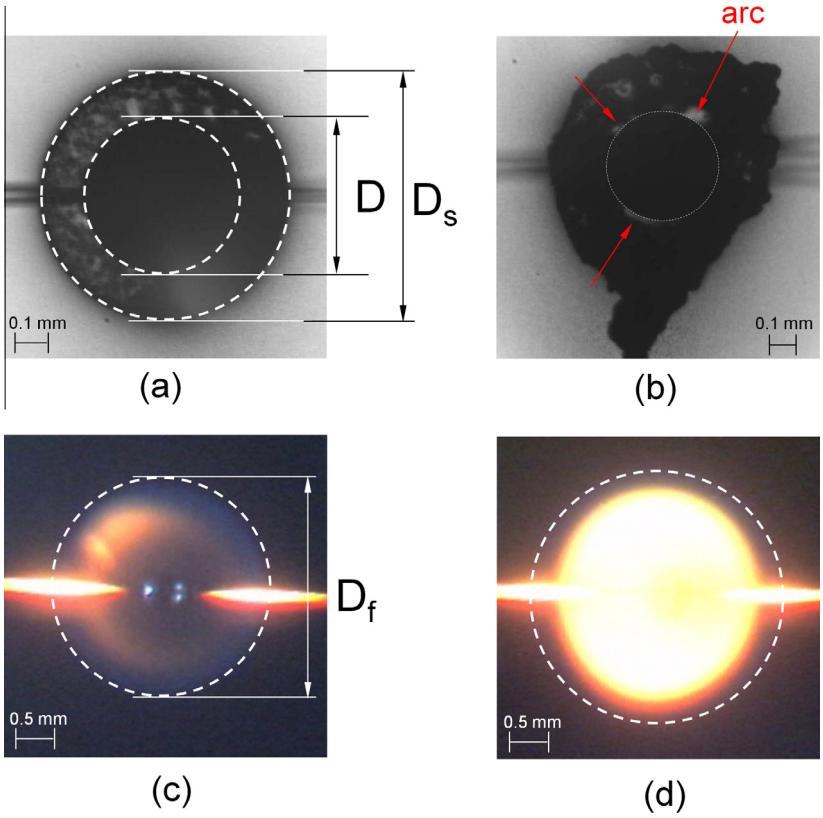

Fig. 3. Illustration of image analyses for (a) D and D_s as determined by manual positioning of virtual ellipse, (b) D as guided by three visible segments, indicated by three arcs, of the droplet boundary, (c) D_f for relatively less sooty HRD using an ellipse, and (d) D_f for luminous flame of R50. The lateral glows in 'c' and 'd' are due to the interaction between the fibers and the flame.

photographed after each experiment with the same settings (e.g., magnification, position from lens, and lighting conditions) as during the free-fall experiment. The calibration ball comprised approximately 392 pixels for BW images and 56 pixels for color images. These scale factors are used to obtain the data reported in the paper.

Regarding measurement uncertainty, the number of pixels that an image encompasses is used to provide an estimate. For the droplet diameter, an initial value of 0.53 is found to comprise approximately 262 pixels as obtained by visual observations from what is best judged as the outer edge of the droplet boundary. The outer edge consists of a "grey transition area" whose thickness depends on the sharpness of the BW image. The thickness for reported images is approximately 5 pixels. As a result, the uncertainty of the boundary of a droplet before it is ignited, in terms of pixel count, would range between 267 and 257 or approximately ± 1.9%. At the other end and well into a burning event, the smallest droplet diameter that could be measured is found to encompass approximately 67 pixels. Using again 5 pixels as the transition area, the uncertainty of the smallest droplet diameters reported here is approximately ±7.5%.

Regarding uncertainty of the soot shell diameter, the largest soot shell measured encompasses approximately 418 pixels and the smallest shell measured consists of about 241 pixels. The soot shell boundary thickness is less well defined compared to the droplet boundary, and approximately 20 pixels is considered to be representative of the soot images reported. The uncertainty of soot shell measurements would then be approximately ± 4.8% at the upper size and ±8.3% at the lower size. Finally, for the flame diameter the largest flame comprises approximately 224 pixels. With a boundary thickness of approximately 8 pixels, the uncertainty of the initial flame pixel count should be about ±3.6% (i.e., +232/224, −216/224). The smallest flame diameter comprises approximately 143 pixels. Taking again a flame boundary thickness of 8 pixels, the uncertainty of a flame diameter is approximately ± 5.6% (i.e., +151/143, −135/143).

2.3. Fuel systems and chemical analysis

Representative fuel properties of the HRD and DF2 fuels are listed in Table 1. DF2 was purchased from LGC Standards (Manchester, NH), while the HRD was provided by Solazyme, Inc. (San Francisco, CA). The 50/50 DF2/HRD mixture was prepared in-house on a volume basis.

The chemical composition of the fuels was determined by gas chromatography-mass spectrometry (GC–MS) analysis using an Agilent Technologies (Santa Clara, CA) 6890N gas chromatograph equipped with an Agilent 7683B autosampler and coupled to a JEOL (Peabody, MA) GCMate II double-focusing sector mass spectrometer. The samples were injected directly without dilution; the injection volume was 0.2 µL. The split/splitless inlet was operated in split flow mode with 200:1 split ratio. Inlet temperature was maintained at 285 °C and the transfer line to the MS was at 290 °C.

The oven program used was as follows: 80 °C for 3 min; ramp to 180 °C at 2 °C/min; ramp to 280 °C at 25 °C/min; and a final hold for 3 min for a total run time of 60 min. The GC column used was a DB-5 MS + DG capillary column (Agilent Technologies) with the dimensions 30 m × 0.25 mm ID, 0.25 µm film thickness and a 10 m DuraGuard guard column section. The MS was operated in positive ion mode at nominal resolving power of 500 (actual 670). Electron impact ionization was used with 70 eV potential

Table 1
Selected properties of fuels examined.

Property	#2 diesel	algal HRD	R50
Formula	$C_{14.0}H_{24.1}$[a]	$C_{15.4}H_{32.7}$[b]	
Stoichiometric coefficient, ν[c]	20.025	23.575	
Molecular weight, *MW* (g/mol)	192.1	217.5	
H/C ratio (moles)	1.72	2.12	
Boiling point (bp, K)	423–653[d]	433–655[e]	
Liquid density, ρ_L (kg/m^3)[f]	816	772	794
Lower heating value (LHV, kJ/kg)	42670[a]	44000[g]	
Cetane number	41.2[a]	~75[g]	
Burning rate, K (mm^2/s)[h]	0.464[i]	0.536[j]	0.509[k]

[a] From Ref. [47].
[b] From Ref. [48].
[c] Assuming 1 mol of fuel and products of CO_2 and H_2O.
[d] From Ref. [49].
[e] From Ref. [50].
[f] Measured at 296.05 K using a digital density meter (Mettler Toledo DA-100M).
[g] From Ref. [28].
[h] Estimated from Fig. 12.
[i] Computed over the range of $0.30 \leqslant t/D_o^2 \leqslant 1.23$ s/mm^2.
[j] Computed over the range of $0.30 \leqslant t/D_o^2 \leqslant 1.35$ s/mm^2.
[k] Computed over the range of $0.30 \leqslant t/D_o^2 \leqslant 1.31$ s/mm^2.

and 200 mA filament current. All analyses were repeated at 240 V, 300 V and 400 V detector voltage to allow for accurate identification and quantitation for both major and minor components.

Mass spectra were acquired from m/z 28 to 500 using a magnetic field sweep with 0.22 s/scan and 0.1 s interscan delay to give 0.32 s total scan duration. Data analysis was performed using TSSPro 3.0 (Shrader Analytical and Consulting Laboratories Inc., Detroit, MI). Component identification was facilitated by the NIST Mass Spectral Database Version 2.0 (NIST, Gaithersburg, MD).

The #2 diesel fuel was found to contain both saturated (73%) and aromatic (27%) hydrocarbons, as shown in Table 2 and Fig. 4. Just two components comprised 70% of the saturated hydrocarbon (SHC) content: tetradecane (50%) and pentadecane (20%). The remaining SHCs were hexadecane (3%) and a very complex mixture of branched hydrocarbons. The aromatic hydrocarbon (ArHC) component in largest abundance was mesitylene (1,3,5-trimethylbenzene, 24% of total ArHC). The remaining ArHCs were comprised of other C_8 to C_{10} alkylbenzenes (48%), and alkyl substituted benzyl and biphenyl derivatives (28%), predominantly with molecular ions with m/z 240 (C_{17}). A trace amount of naphthalene was also detected. This composition is consistent with the highly sooting propensity of diesel fuel.

The total ion chromatogram (TIC) of GC–MS of algal renewable diesel is shown in Fig. 5 and the composition is listed in Table 3. The HRD contained exclusively saturated hydrocarbons with no detectable aromatic components, even at trace level. C_{15} to C_{18} SHCs constituted 95% of the sample with C_{17} as the predominant component (51%) followed by C_{18} (23%) as well as C_{15} and C_{16} (10% each). The sample also contained minor (<2%) amounts of C_8 to C_{14} as well as C_{19} HCs. Within each SHC series, the straight chain isomer was dominant (40–50%) followed by a uniform distribution of all possible methyl-branched isomers (30–45% combined) and smaller amounts of more highly branched isomers (15–25%).

3. Results

The primary "data" are qualitative visualizations of the droplet burning history recorded by the two cameras. The quantitative measurements are then obtained from these video images. As such, the quality of the video images is extremely important in order to obtain accurate and precise measurements. Fig. 6 compares flame-illuminated images at 0.1 s intervals for HRD, R50, and DF2, while Fig. 7 shows backlighted images of these fuels.

Table 2
Composition of #2 diesel determined by GC–MS.

Compound class	Composition of fuel	
Component	% of compound class	% of Total
Saturated Hydrocarbons	–	73%
Tetradecane	50%	37%
Pentadecane	20%	15%
Hexadecane	3%	2%
Other	27%	20%
Aromatics	–	27%
Mesitylene	24%	7%
Other alkylbenzenes	44%	12%
Alkylated biaromatics	32%	8%

The flame structure consists of an inner yellow zone and a fainter outer blue zone. The yellow zone, observed to varying extent in all experiments, is due to incandescence of soot aggregates that reside between the droplet and the flame. Flame brightness, a qualitative measure of the sooting propensity, is shown in Fig. 6, and is highest for DF2, in the order (high to low) of DF2 > R50 > HRD. This observation is consistent with clear differences in the amount of soot formed for droplets of ostensibly the same size as shown in Fig. 7. The different aromatic content can be responsible for this difference. The chemical analysis discussed previously shows a high concentration of aromatic species, well known soot-forming constituents, in DF2 (27%), whereas HRD has virtually none. As such, greater apparent thickness of the soot shell and brighter flame for DF2 are observed.

Some initial asymmetry of the droplet flames exists (e.g., Fig. 6b and c, R50 and DF2 at 0.1 s respectively) due to gas motion induced by spark ignition and electrode retraction. This asymmetry could cause the formation of large soot aggregates, which are less susceptible to stay locked in the soot shell and can drift outward, as shown in Figs. 6c and 7c (DF2 at 0.2 s). But this initial asymmetry does not affect the spherically symmetry in the later portion of the burning history. Two horizontal needle-like glows observed on either side of the flames are caused by the interaction between the flame and the support fibers.

Fig. 7 shows droplet and soot structures that are consistent with the schematics in Fig. 1. The development of the soot shell is clearly indicated. Soot aggregates are trapped between the droplet and the flame, where forces acting on them balance [34]. This effect is clearly visible in Fig. 7. As burning proceeds, the aggregates become so numerous that they form connected structures and lose their character as free-floating entities.

Fig. 8a shows the measured evolution of droplet diameter for one HRD test. Droplet diameter measurements are presented using the coordinates from the quasi-steady scaling of droplet burning [41]: $(D/D_o)^2$ for size and t/D_o^2 for time. The initial fluctuations seen in this run within first 0.15 s/mm^2 are due to droplet deformation induced by spark energy at the onset of this burning. However, this initial disturbance does not affect the reminder of burning. In addition, the slight increase observed in the droplet diameter within the first 0.25 s/mm^2 is a result of initial droplet heating.

The trend in Fig. 8 shows that the scaled diameter decreases until a certain time after which the droplet sizes start to slightly increase. At a certain point (e.g., time "B" in Fig. 8a and b), droplet diameter dramatically decreases, suggesting a sudden mass ejection from the fuel droplet. This behavior is like the micro-explosion effect which has been previously discussed in Refs. [42,43]. In the present study, we believe that this effect is due to formation of a bubble within the droplet, most likely on the support fiber, that ejects mass in the process. Fig. 8b presents consecutive images recorded by the BW camera illustrating this effect, which is observed in all of the experiments in this study for all

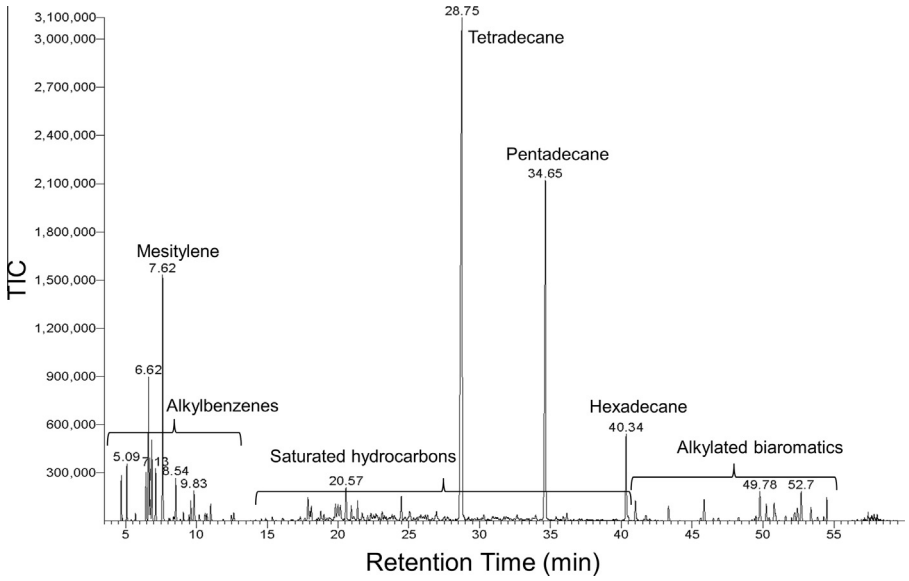

Fig. 4. Total ion chromatogram (TIC) of GC–MS analysis of #2 diesel fuel at 300 V detector voltage. Peaks labeled with retention times represent straight chain hydrocarbons.

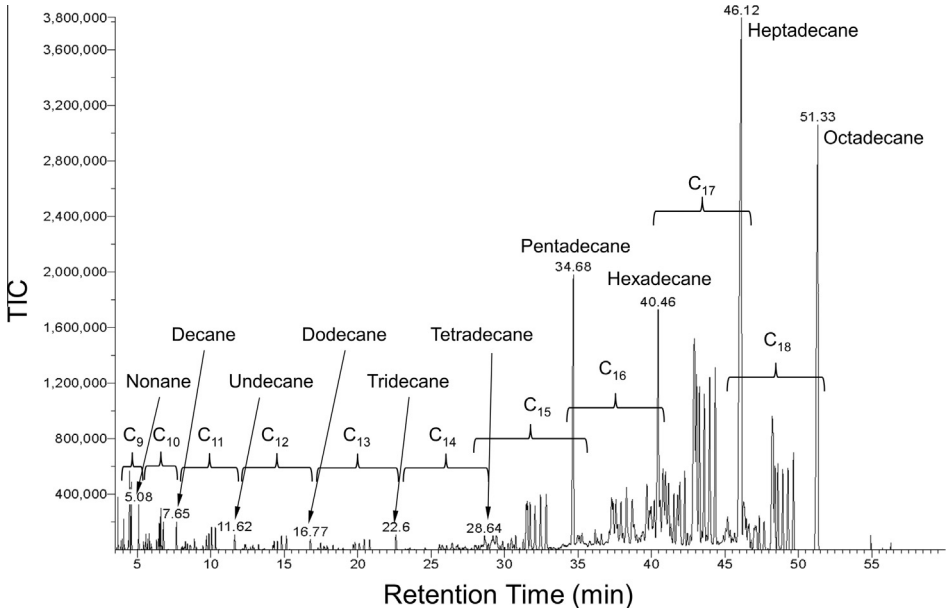

Fig. 5. Total ion chromatogram of GC–MS analysis of algal hydrotreated renewable diesel fuel at 300 V detector voltage. Peaks labeled with retention times represent straight chain hydrocarbons. C_n indicates isomers of saturated hydrocarbons with 'n' carbon atoms.

three fuels examined. Note that such an event is not predictable. It could occur either in the middle of the droplet burning process or near the end of a burn.

Fig. 8c illustrates the effect of internal bubbling in the D^2 plot. The fuel droplet is burning and the diameter is decreasing in the initial portion of the burning history. Then there is a slight increase in the evolution of droplet diameter (as indicated by the red line), suggesting the bubble formation and growth inside the fuel droplet. The droplet diameter will then dramatically decrease due to the ejection of mass from the fuel droplet. If there were no internal bubbling, the evolution of the droplet diameter will follow the trend of the blue dash line and the droplet will burn to completion without any sudden decrease of the diameter.

It is interesting that the bubble formation and mass ejection observed here did not seem to happen for gasoline (bp 305.7–471.6 K) [44] nor Jet-A (bp, 478–573 K) [45] with the same experimental setup and procedure. A potential explanation of this behavior is provided as follows and Fig. 9 is a schematic to illustrate this process. The range of the boiling point for fuels examined in this study is wider (i.e., Table 1, DF2, bp 423–653 K, with a bp range of 230 K and HRD, bp 433–655 K, with a bp range of 222 K) compared to gasoline (with a bp range of 165.9 K) and Jet-A (with a bp range of 95 K). In addition, one could envision an approximate range of boiling point for R50 (with a range of ~230 K) based on boiling points of HRD and DF2 since R50 is an equi-volume mixture of them. This wide range of boiling points for all fuels investigated in this study would facilitate bubble nucleation and growth inside the fuel droplet since a preferential vaporization effect can occur and the temperature of the fuel droplet will change (likely to increase) throughout the burning

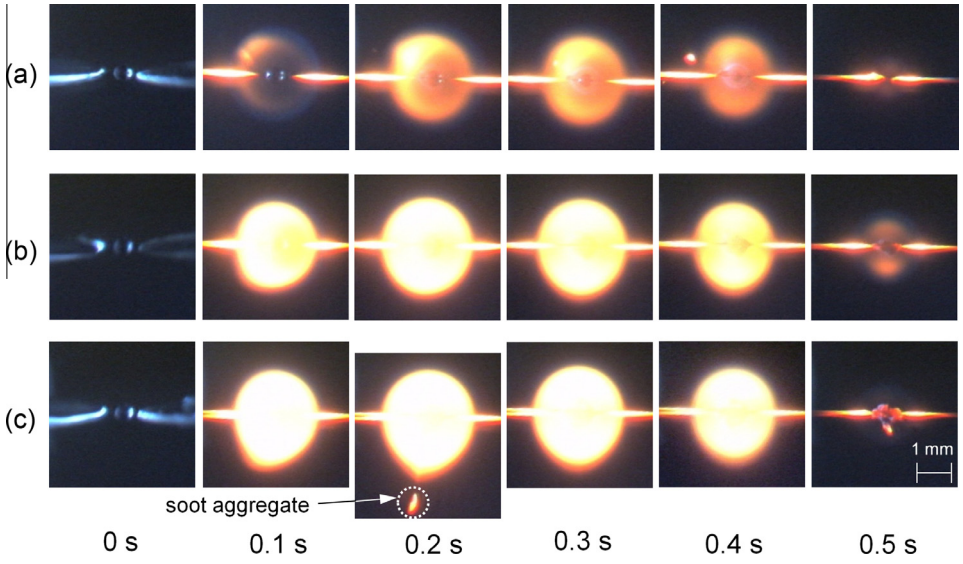

Fig. 6. Selected color images showing spherical droplet flames for: (a) HRD (D_o = 0.52 mm), (b) R50 (D_o = 0.55 mm), and (c) DF2 (D_o = 0.53 mm). The horizontal glows on either side of the flames arise from the flame contacting the support fibers.

Table 3
Composition of algal renewable diesel determined by GC–MS.

Series	Total	Composition of series		
		Straight Chain (%)	Methyl branched (%)	Other (%)
C_8	Trace	–	–	–
C_9	1.3%	–	–	–
C_{10}	1.1%	–	–	–
C_{11}	0.9%	–	–	–
C_{12}	0.7%	–	–	–
C_{13}	0.7%	–	–	–
C_{14}	0.3%	–	–	–
C_{15}	10.8%	44.0	30.9	25.1
C_{16}	10.1%	38.6	46.2	15.2
C_{17}	50.4%	44.5	30.7	24.8
C_{18}	22.5%	51.0	33.9	15.2
C_{19}	1.2%	–	–	–

history. At some point, if one constituent does not evaporate completely when the temperature of the droplet is at its boiling point, with continuous increase of the temperature at the droplet surface, this constituent will be trapped inside the droplet and start to boil forming bubbles inside the fuel droplet. The presence of the support fiber facilitates the formation of bubbles since it provides the sites where bubbles can initially form (cf. Fig. 9b). The bubble formed inside the droplet will continue to grow (Fig. 9c) with the burning of the droplet until it finally ejects mass from the fuel droplet as shown in Figs. 8b and 9d. This mass ejection process can distort the spherical symmetry of the soot shell (as shown in Figs. 8b and 9d) since soot particles can be blown away during the mass ejection event.

Fig. 10 shows the measured evolution of droplet diameter from all experiments performed for HRD, R50, and DF2 (the data are

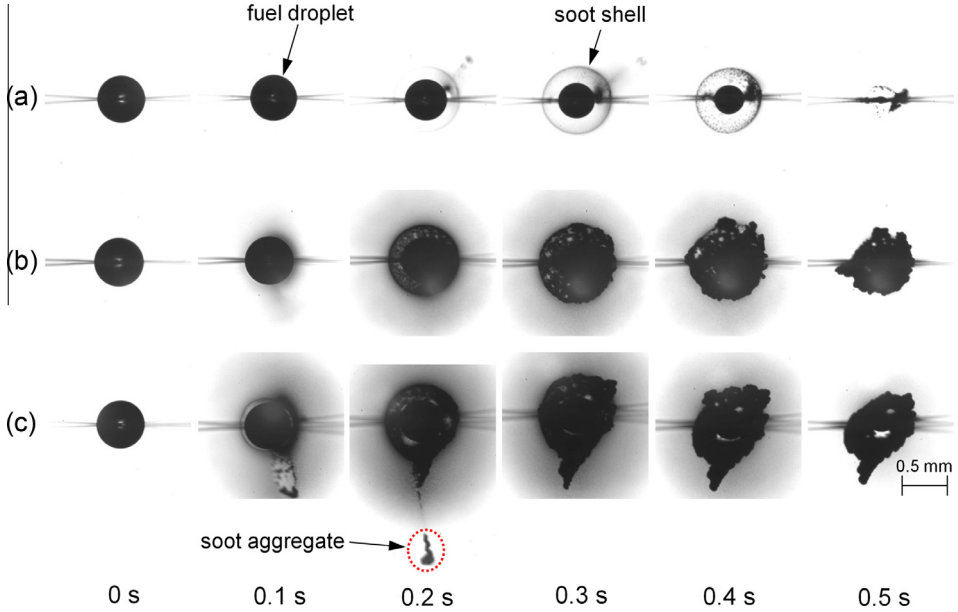

Fig. 7. Selected BW images highlighting droplet and soot dynamics: (a) HRD (D_o = 0.52 mm), (b) R50 (D_o = 0.55 mm), and (c) DF2 (D_o = 0.53 mm).

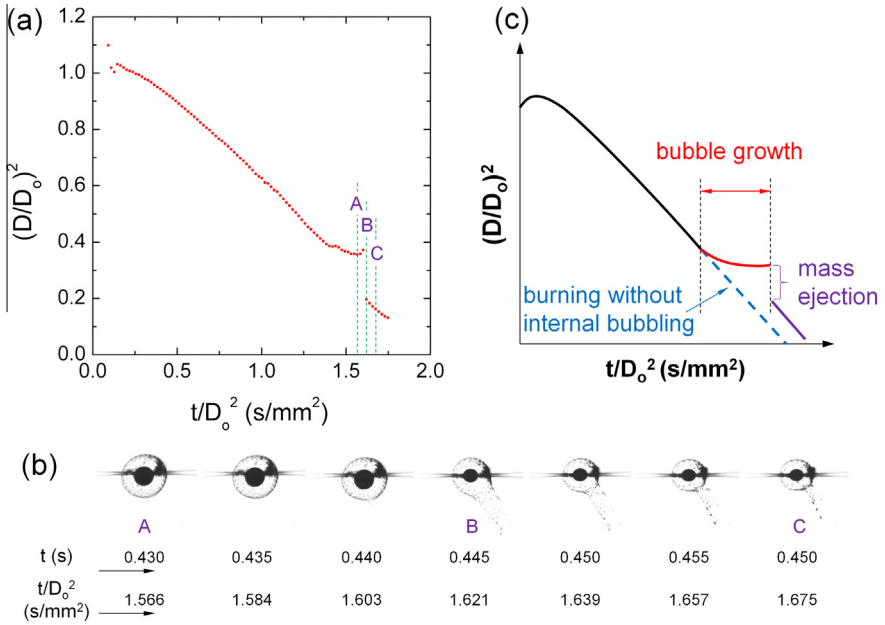

Fig. 8. Illustration of an internal bubbling and mass ejection events for a HRD droplet (D_o = 0.52 mm): (a) measured evolution of the droplet diameter, (b) consecutive BW images showing internal bubbling and mass ejection, and (c) schematic of the droplet diameter evolution with and without internal bubbling.

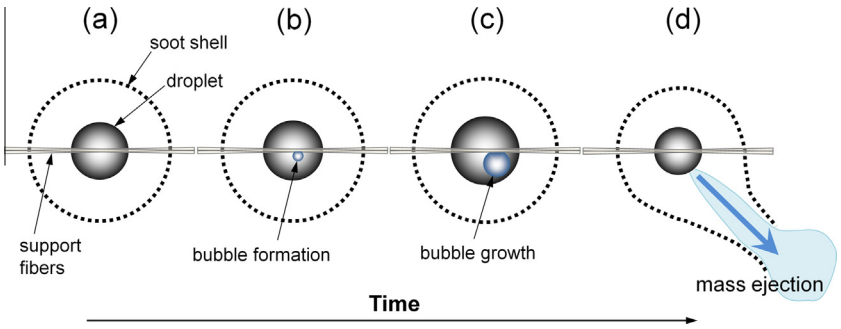

Fig. 9. Schematic of the internal bubbling and mass ejection events: (a) a burning droplet prior to the bubble formation; (b) a bubble formed inside the fuel droplet, (c) bubble growth inside the droplet, and (d) mass being ejected from the fuel droplet.

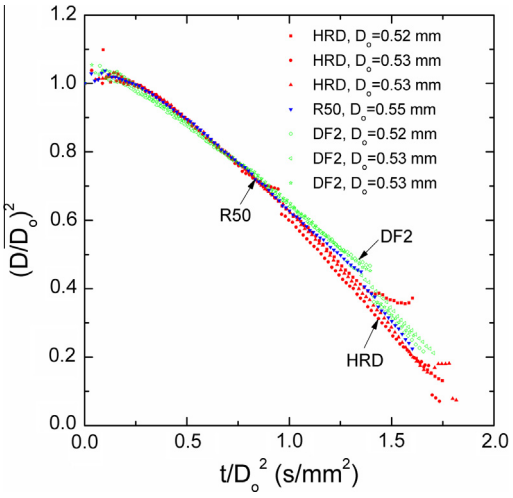

Fig. 10. Evolution of the droplet diameter from individual experiments for all fuels examined in the present study.

included in the Supplementary Material). In Fig. 10, the data are also presented using scaled coordinates as discussed previously. In these coordinates, the slope corresponds to the burning rate ($K \equiv |d(D/D_o)^2/d(t/D_o^2)|$), which measures the combustion rate of a given fuel. As shown in Fig. 10, the mass ejection event is observed for each individual experiment in this study. Prior to this

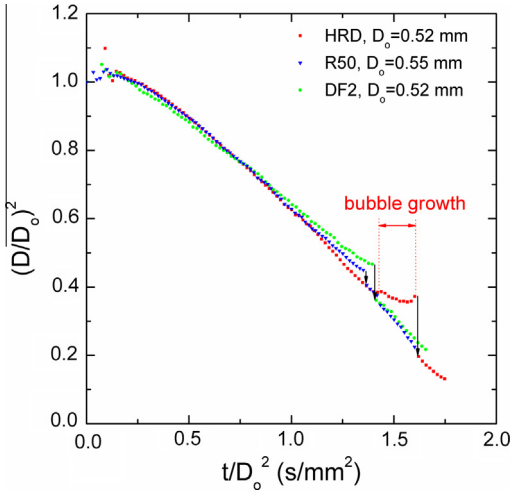

Fig. 11. Evolution of the droplet diameter from one selected experiment for each fuel examined in the present study. Black arrows indicate the reduction of droplet diameter due to internal boiling that ejected mass during the burning process.

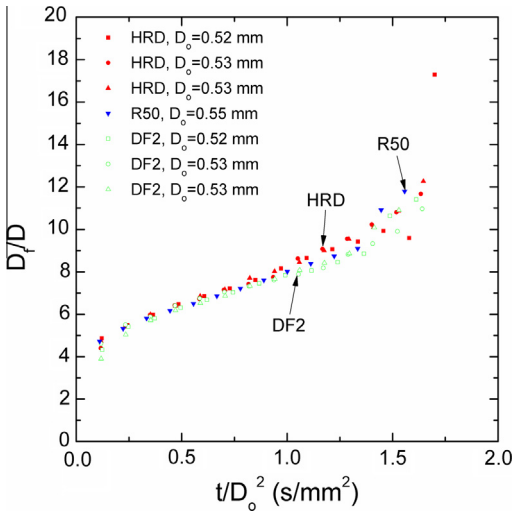

Fig. 12. Evolution of the flame standoff ratio for all fuels examined in the present study.

event, results on the same fuel show the repeatability of the experiments.

Due to the presence of internal bubbling, which introduces significant scatter in the data, averaging the droplet diameters for all experiments performed on the same fuel for the purpose of comparing the various fuels with one another is not appropriate. Instead, only one representative test is selected from each of the fuels, and the evolutions of droplet diameter of the three different fuels are compared. Fig. 11 presents the evolution of droplet diameter for these selected results and black arrows show the mass ejection events for each test. The bubble growth period for the HRD test is also indicated in Fig. 11.

Linearizing the measurements from 0.3 s/mm^2 to the time prior to the mass ejection event gives the burning rates listed in Table 1. Different end times are selected for this linear fit to obtain burning rates since the ejection occurs at different times for each fuel. The time ranges for the linearization of results for each fuel are given in Table 1. HRD appears to have a slightly higher burning rate than DF2. The tests plotted in Fig. 11 are selected because the mass ejection occurs near the end of a burning history (after 1.25 s/mm^2) which permits a linear fit of the droplet diameter data over a long period of time (0.3 to ~1.25 s/mm^2, as presented in Table 1) for each fuel to obtain a reliable comparison of burning rates. The experiments performed on each fuel are fairly repeatable prior to the mass injection event, as shown by measurements of droplet diameters from different test runs for the same fuel (i.e., Fig. 10).

The flame standoff ratio (FSR, D_f/D), which signifies the relative distance of the droplet to the flame, is shown in Fig. 12. It is clear that the relative position of the flame to the droplet increases with time during the droplet burning history (the decrease of FSR in Fig. 12 observed after 1.5 s/mm^2 is due to the influence of bubble formation and mass ejection events, prior to which measurements of D slightly increases because of bubble growing inside the droplet, resulting in a decrease of flame standoff ratio). As shown in Fig. 12, HRD produces flames that are slightly further away from the droplet compared to DF2 droplet flames. The FSR for R50 resides in between HRD and DF2, as expected.

The trends noted above can be explained by a scale analysis. According to the classical D^2 burning law [41], the quasi-steady burning rate is proportional to fuel properties as

$$K \sim \frac{k_g/c_{p,g}}{\rho_L} \tag{1}$$

Both HRD and DF2 are hydrocarbon fuels (cf. Figs. 4 and 5) whose thermal properties are not substantially different. As such, the liquid density in Eq. (1) becomes the controlling parameter: $K \sim 1/\rho_L$.

Defining $\Phi_K \equiv K_{\mathrm{HRD}}/K_{\mathrm{DF2}}$, we can write

$$\Phi_K \sim \frac{\rho_{\mathrm{L,DF2}}}{\rho_{\mathrm{L,HRD}}} \tag{2}$$

Using the liquid density values in Table 1 gives $\Phi_K \sim 1.06$. With the experimentally measured burning rates in Tables, $\Phi_K \sim 1.16$. Given the simplifications involved in the scaling analysis and uncertainty of the burning rate measurements, these results are found to be consistent with one another. More importantly, the scaling analysis confirms that the burning rate of HRD is slightly higher than that of DF2, which is consistent with the observations in Fig. 11. Note that only HRD and DF2 are compared because they bound the burning rate of R50 as shown in Figs. 10 and 11.

It has been previously reported that *n*-butanol, also known as a bio-derived fuel, has the same burning rate as gasoline [44]. In this study, the burning rate of algal HRD is found to be similar to #2 diesel. These results are interesting since they may suggest that bio-derived fuels have the capability of match the burning characteristics of real transportation fuels.

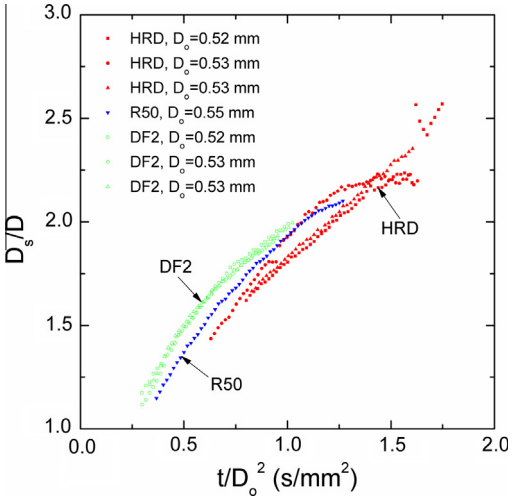

Fig. 13. Evolution of the soot standoff ratio for all fuels examined in the present study.

Regarding the flame standoff ratio, the classical theory of FSR as extended by Aharon and Shaw [46] is used to show that, for HRD and DF2

$$\Phi_F \equiv \frac{(D_f/D)_{HRD}}{(D_f/D)_{DF2}} \sim \left(\frac{\rho_{L,HRD}}{\rho_{L,DF2}}\right)\left(\frac{K_{HRD}}{K_{DF2}}\right)\left(\frac{v_{HRD}}{v_{DF2}}\right)\left(\frac{MW_{DF2}}{MW_{HRD}}\right) \quad (3)$$

With values from Table 1, we find that $\Phi_F \sim 1.14$. This result suggests that HRD should have a slightly higher FSR than DF2, which is consistent with Fig. 12, though the differences in Fig. 12 are much smaller. This may be due to the approximate nature of the theory and/or uncertainties in estimating the variable values in Eq. (3).

The relative position of the soot shell to the droplet, that is, soot standoff ratio (SSR, D_s/D), is shown in Fig. 13. The SSR also follows the time dependence of FSR: as the FSR increase with time during the burning, so too does the soot standoff ratio. As shown in Fig. 13, the SSR is also slightly affected by internal bubbling effect (e.g. HRD at $\sim$1.7 s/mm^2). As expected and on the basis of Figs. 12 and 13, the soot shell resides between the droplet and the flame (i.e., SSR < FSR) since soot will only form on the fuel-rich side of the droplet diffusion flame.

4. Conclusions

The droplet combustion characteristics of hydrotreated renewable diesel derived from algae, conventional #2 diesel, and an algal renewable diesel/#2 diesel mixture are compared for the base case of droplet burning in an environment that promotes spherical droplet flames. The results show that renewable diesel and R50 droplets have burning rates that are very close to the conventional #2 diesel and that hydrotreated renewable diesel and R50 droplet flames reside farther from the droplet surface than #2 diesel droplet flames. Scaling analyses from the quasi-steady theory suggest that fuel properties are important in evaluating the burning rate and flame position of the fuels and the results from the scale arguments are consistent with the experimental trends obtained. The sooting propensities of fuels examined are in the order of (high to low) #2 diesel > R50 > algae renewable diesel, which is consistent with the observations of flame brightness, with #2 diesel having the brightest flame.

The results presented here are consistent with HRD derived from algae being an attractive additive or even a drop-in replacement to petroleum-base diesel fuel. The results also suggest that the HRD may reduce particulate emissions during the combustion based on its lower sooting propensity compared to #2 diesel.

Acknowledgements

This work was supported in part by Cornell University's David R. Atkinson Center for a Sustainable Future (ACSF) under an Academic Venture Fund (AVF) grant, and by the National Aeronautics and Space Administration (NASA) under Grants NNX15AB33G and NNX008AI51G with Dr. Graham Kerslick of Cornell and Mr. Michael Hicks as the Project Monitors. The authors are also pleased to acknowledge Prof. Francis J. DiSalvo of the Department of Chemistry and Chemical Biology for his interest in our work and for assisting in developing the collaborative team. The interest of Prof. Charles Greene, and the assistance of Ms. Meilin Dong of Cornell with some of the experimental work, is also greatly appreciated.

Appendix A. Supplementary material

Supplementary data associated with this article can be found, in the online version, at http://dx.doi.org/10.1016/j.fuel.2015.11.036.

References

[1] Knothe G. A technical evaluation of biodiesel from vegetable oils vs. algae. Will algae-derived biodiesel perform? Green Chem 2011;13:3048–65.
[2] Rakopoulos CD, Rakopoulos DC, Hountalas DT, Giakoumis EG, Andritsakis EC. Performance and emissions of bus engine using blends of diesel fuel with biodiesel of sunflower or cottonseed oils derived from Greek feedstock. Fuel 2008;87:147–57.
[3] Rakopoulos DC, Rakopoulos CD, Giakoumis EG, Dimaratos AM, Founti MA. Comparative environmental behavior of bus engine operating on blends of diesel fuel with four straight vegetable oils of Greek origin: sunflower, cottonseed, corn and olive. Fuel 2011;90:3439–46.
[4] Qi DH, Geng LM, Chen H, Bian YZ, Liu J, Ren XC. Combustion and performance evaluation of a diesel engine fueled with biodiesel produced from soybean crude oil. Renew Energy 2009;34:2706–13.
[5] Chisti Y. Biodiesel from microalgae. Biotechnol Adv 2007;25:294–306.
[6] Zaimes GG, Khanna V. Environmental sustainability of emerging algal biofuels: a comparative life cycle evaluation of algal biodiesel and renewable diesel. Environ Prog Sustain Energy 2013;32:926–36.
[7] Huo H, Wang M, Bloyd C, Putsche V. Life-cycle assessment of energy use and greenhouse gas emissions of soybean-derived biodiesel and renewable fuels. Environ Sci Technol 2009;43:750–6.
[8] Borkowski MG, Zaimes GG, Khanna V. Integrating LCA and thermodynamic analysis for sustainability assessment of algal biofuels: Comparison of renewable diesel vs. biodiesel. Sustainable Systems and Technology (ISSST), 2012 IEEE International Symposium on, Boston, MA, May 16–18, 2012.
[9] Bharathiraja B, Chakravarthy M, Kumar RR, Yuvaraj D, Jayamuthunagai J, Kumar RP, et al. Biodiesel production using chemical and biological methods – a review of process, catalyst, acyl acceptor, source and process variables. Renew Sustain Energy Rev 2014;38:368–82.
[10] Urooj S, Hussain A, Srivastava N. Biodiesel production from algal blooms: a step towards renewable energy generation & measurement. Int J Meas Technol Instrum Eng 2012;2:60–71.
[11] Beal CM, Hebner RE, Webber ME, Ruoff RS, Seibert AF, King CW. Comprehensive evaluation of algal biofuel production: experimental and target results. Energies 2012;5:1943–81.
[12] Tang H, Abunasser N, Garcia MED, Chen M, Simon Ng KY, Salley SO. Potential of microalgae oil from Dunaliella tertiolecta as a feedstock for biodiesel. Appl Energy 2011;88:3324–30.
[13] Li Y, Lian S, Tong D, Song R, Yang W, Fan Y, et al. One-step production of biodiesel from Nannochloropsis sp. on solid base Mg–Zr catalyst. Appl Energy 2011;88:3313–7.
[14] Heilmann SM, Jader LR, Harned LA, Sadowsky MJ, Schendel FJ, Lefebvre PA, et al. Hydrothermal carbonization of microalgae II. Fatty acid, char, and algal nutrient products. Appl Energy 2011;88:3286–90.
[15] Levine RB, Pinnarat T, Savage PE. Biodiesel production from wet algal biomass through in situ lipid hydrolysis and supercritical transesterification. Energy Fuels 2010;24:5235–43.
[16] Johnson MB, Wen Z. Production of biodiesel fuel from the microalga schizochytrium limacinum by direct transesterification of algal biomass. Energy Fuels 2009;23:5179–83.
[17] Jung EE, Kalontarov M, Doud DF, Ooms MD, Angenent LT, Sinton D, et al. Slab waveguide photobioreactors for microalgae based biofuel production. Lab Chip 2012;12:3740–5.
[18] Wang W-C, Allen E, Campos AA, Cade RK, Dean L, Dvora M, et al. ASI: Dunaliella marine microalgae to drop-in replacement liquid transportation fuel. Environ Prog Sustain Energy 2013;32:916–25.
[19] Hoekman SK, Gertler AW, Broch A, Robbins C, Natarajan M. Biodistillate transportation fuels 1. Production and properties. SAE Int J Fuels Lubr 2009;2:185–232.
[20] Blakey S, Rye L, Wilson CW. Aviation gas turbine alternative fuels: a review. Proc Combust Inst 2011;33:2863–85.
[21] Wahlen BD, Morgan MR, McCurdy AT, Willis RM, Morgan MD, Dye DJ, et al. Biodiesel from microalgae, yeast, and bacteria: engine performance and exhaust emissions. Energy Fuels 2013;27:220–8.
[22] Haik Y, Selim MYE, Abdulrehman T. Combustion of algae oil methyl ester in an indirect injection diesel engine. Energy 2011;36:1827–35.
[23] Fisher BC, Marchese AJ, Volckens J, Lee T, Collett JL. Measurement of gaseous and particulate emissions from algae-based fatty acid methyl esters. SAE Int J Fuels Lubr 2010;3:292–321.
[24] Jayaprabakar J, Karthikeyan A. Analysis on the performance, combustion and emission characteristicsof a CI engine fuelled with algae biodiesel. Appl Mech Mater 2014;591:33–7.
[25] Rinaldini CA, Mattarelli E, Magri M, Beraldi M. Experimental investigation on biodiesel from microalgae as fuel for diesel engines. 2014. SAE International, 2014-01-1386.
[26] Patel JS, Kumar N, Deep A, Sharma A, Gupta D. Evaluation of emission characteristics of blend of algae oil methyl ester with diesel in a medium capacity diesel engine. 2014. SAE International, 2014-01-1378.
[27] Groenewegen J-R, Sidhu S, Hoke J, Wilson C, Litke P. The performance and emissions effects of utilizing heavy fuels and algae based biodiesel in a port-fuel-injected small spark ignition internal combustion engine. 47th AIAA/ASME/SAE/ASEE Joint Propulsion Conference & Exhibit, San Diego, CA, July 31 – August 3, 2011. American Institute of Aeronautics and Astronautics, AIAA 2011–5807.

[28] Petersen J, Seivwright D, Caton P, Millsaps K. Combustion characterization and ignition delay modeling of low- and high-cetane alternative diesel fuels in a marine diesel engine. Energy Fuels 2014;28:5463–71.
[29] Caton PA, Williams SA, Kamin RA, Luning-Prak D, Hamilton LJ, Cowart JS. Hydrotreated algae renewable fuel performance in a military diesel engine. Proc. ASME 2012 Internal Combustion Engine Division Spring Technical Conference, p. 121–32.
[30] Quiñones M, Leung R, Williams S. Algae based hydroprocessed fuel use on a marine gas turbine. J Eng Gas Turbines Power 2012;134:122201.
[31] MacKinnon MT, Shaw JD, Quiñones M. Combustion assessment of a 50% Algae-Based HRD76 Fuel and 50% conventional F76 military diesel fuel blend. J Eng Gas Turbines Power 2012;134:121501.
[32] Alam FE, Liu YC, Avedisian CT, Dryer FL, Farouk TI. N-Butanol droplet combustion: numerical modeling and reduced gravity experiments. Proc Combust Inst 2015;35:1693–700.
[33] Farouk TI, Dryer FL. On the extinction characteristics of alcohol droplet combustion under microgravity conditions – a numerical study. Combust Flame 2012;159:3208–23.
[34] Jackson GS, Avedisian CT, Yang JC. Observations of soot during droplet combustion at low gravity: heptane and heptane/monochloroalkane mixtures. Int J Heat Mass Transfer 1992;35:2017–33.
[35] Sirignano WA. Dynamics and transport of droplets and sprays. Cambridge, UK: Cambridge Univeristy Press; 1999. p. 10–21.
[36] Kalnes T, Marker T, Shonnard DR. Green diesel: a second generation biofuel. Int J Chem React Eng 2007;5:1542–6580.
[37] Liu YC, Avedisian CT. A comparison of the spherical flame characteristics of sub-millimeter droplets of binary mixtures of n-heptane/iso-octane and n-heptane/toluene with a commercial unleaded gasoline. Combust Flame 2012;159:770–83.
[38] Liu YC, Xu Y, Avedisian CT, Hicks MC. The effect of support fibers on micro-convection in droplet combustion experiments. Proc Combust Inst 2015;35:1709–16.
[39] Avedisian CT, Callahan BJ. Experimental study of nonane/hexanol mixture droplet combustion without natural or forced convection. Proc Combust Inst 2000;28:991–7.
[40] Dembia CL, Liu YC, Avedisian CT. Automated data analysis for consecutive images from droplet combustion experiments. Image Anal Stereology 2012;31:137–48.
[41] Turns SR. An introduction to Combustion. 3rd ed. New York: McGraw-Hill; 2012. p. 396.
[42] Yang JC, Jackson GS, Avedisian CT. Combustion of unsupported methanol/dodecanol mixture droplets at low gravity. Symp (Int) Combust 1991;23:1619–25.
[43] Jackson GS, Avedisian CT. Combustion of unsupported water-in-n-heptane emulsion droplets in a convection-free environment. Int J Heat Mass Transfer 1998;41:2503–15.
[44] Xu Y, Avedisian CT. Combustion of n-butanol, gasoline, and n-butanol/gasoline mixture droplets. Energy Fuels 2015;29:3467–75.
[45] Liu YC, Savas AJ, Avedisian CT. Spherically symmetric droplet combustion of three and four component miscible mixtures as surrogates for Jet-A. Proc Combust Inst 2013;34:1569–76.
[46] Aharon I, Shaw BD. On the roles of thermal diffusion and distinct binary diffusion coefficients in modeling droplet flame locations in microgravity. Microgravity Sci Technol 1997;10:75–85.
[47] Rothamer DA, Murphy L. Systematic study of ignition delay for jet fuels and diesel fuel in a heavy-duty diesel engine. Proc Combust Inst 2013;34:3021–9.
[48] Gowdagiri S, Wang W, Oehlschlaeger MA. A shock tube ignition delay study of conventional diesel fuel and hydroprocessed renewable diesel fuel from algal oil. Fuel 2014;128:21–9.
[49] LGC Standards. Safety Data Sheet, #2 Diesel Fuel, < 3ppm Sulfar. 2014, VHG-DSL-1GAL.
[50] Solazyme Inc., Safety Data Sheet, SoladieselRD. 2014, C-R-00259-000.